Available online at www.sciencedirect.com
ScienceDirect
Journal of Sound and Vibration 306 (2007) 849–864
JOURNAL OF SOUND AND VIBRATION
www.elsevier.com/locate/jsvi

A new finite element model for piezothermoelastic composite beam

Jian Ping Jiang*, Dong Xu Li

College of Aerospace and Material Engineering, National University of Defense Technology, Changsha, Hunan Province 410073, China

Received 19 September 2006; received in revised form 1 April 2007; accepted 30 June 2007

Abstract

Finite element modelling of piezothermoelastic composite beam with distributed piezoelectric sensor and actuator layers is considered in this paper. The mathematical model is based on a high-order displacement field, a new high-order electrical potential field and a linear temperature field. This model is developed for a composite beam structures using generalized virtual work principle and is facilitated by two nodes Hermitian beam element. Constant-gain negative velocity feedback control approach has been used for active vibration control with the structures subjected to impulse and thermal excitations. The influence of the pyroelectric effects on the vibration control performance is also investigated. Comparison of numerical results from this formulation with previous works, PVDF bimorph beam, shows that the present modelling method is very efficient. Additional numerical studies for piezothermoelastic composite beam demonstrate capabilities of the current formulation to predict the thermal deformation of composite beams, as well as the active compensation of these deformations using piezoelectric structures.

1. Introduction

The development of intelligent composite materials with piezoelectric components offers great potential for use in advanced aerospace structural applications. The coupled electromechanical properties of piezoelectric ceramics and their availability in the form of thin sheets make them well suited for use as distributed sensors and actuators for controlling structural response. In the sensors application, mechanically or thermally induced deformations can be determined from measurement of the induced electrical potential (*direct piezoelectric effect*), whereas in actuator applications deformation of strain can be controlled through the introduction of appropriate electric potential (*converse piezoelectric effect*). By integrating distributed piezoelectric sensors/actuators and advanced composites, the potential exists for forming high-strength, high-stiffness, lightweight structures capable of self-monitoring and self-controlling. Typical applications of such structure are envisioned in the thermal distortion management of propulsion components and/or space structures. Before they can be utilized in these applications, however, the performance of piezoelectric

*Corresponding author.
E-mail address: jianping202@163.com (J.P. Jiang).

0022-460X/$ - see front matter © 2007 Elsevier Ltd. All rights reserved.
doi:10.1016/j.jsv.2007.06.023

structures in thermal environment must be quantified. Consequently, this paper will present the development of comprehensive mechanics for the analysis of such piezoelectric thermal structures.

There have been various mathematical models developed to describe the behavior of the structure that is actuated and sensed by piezoelectric materials attached/bonded to it. These models can be classified into three broad categories as induced strain models (Crawley and Luis [1], Tzou and Gadre [2], Wang and Rogers [3], and Sung et al. [4]), coupled electromechanical models (Mitchell and Reddy [5], Tzou and Tseng [6], Saravanos and Heyliger [7], and Heyliger et al. [8]) and coupled piezothermoelastic models (Tzou and Bao [9], Chandrashekhara and Tenneti [10], and Sunar and Rao [11]).

The induced strain models use approximate theories to incorporate the piezoelectric effects and are generally limited to predicting only the active response of piezoelectric materials since the electric potential is neglected as a state variable in the formulation. However, the limitation is found in the induced strain models and arises from the use of approximate forces to represent the piezoelectric strains. This approximate representation fails to capture the coupled mechanical and electrical response and limits these models for use in predicting only the actuator behavior of piezoelectric materials.

The coupled electromechanical models provide a more consistent representation of both the sensory and active responses of piezoelectric materials by incorporating both the displacements and electric potential as state variables in the formulation. Typically, these models are implemented as finite element codes to provide a more general analysis tool and a wide variety of different beam, plate, shell, and solid elements have been developed. The induced strain limitations are overcome in the coupled electromechanical models through the use of a more consistent representation of the coupling, which occurs between the electrical and mechanical responses. However, the thermal effects are neglected.

A natural extension of the coupled electromechanical models is to also incorporate thermal effects. These coupled thermoelectromechanical models include temperature as an additional state variable to account for thermal effects in addition to the piezoelectric effects. Thermal effects become important when the piezoelectric structure has to operate in either extremely hot or cold temperature environments, e.g. space. These extreme conditions may severely affect the response of piezoelectric structures in three distinct ways: (1) induction of thermal stresses resulting from differences in the coefficients of thermal expansion; (2) pyroelectric phenomena; and (3) temperature dependence of the elastic, piezoelectric, and dielectric properties.

Recently, an increasing number of investigations have addressed piezothermoelasticity. Among the investigations in piezothermoelasticity, the static and dynamic problems of different structures are discussed (Tauchert et al. [12]). A coupled thermo-piezoelectric-mechanical model of composite laminates with surface bonded piezoelectric actuators was developed (Chattopadhyay et al. [13] and Jingmei et al. [14]). A general solution for dynamic piezothermo-elastic problems of transversely isotropic piezoelectric materials is derived (Haojiang et al. [15]). Altay and Dökmeci [16] formulated the fundamental equations of thermopiezoelectricity with second sound in variational form, and systematically derived the system of one-dimensional (1D) equations for the high-frequency vibrations of a cylindrical rod. The numerical and experimental study of active compensation of thermal deformation of a composite beam using piezoelectric ceramic actuators was considered (Song et al. [17]). Altay and Dökmeci [18] modified the Mindlin's equations of thermopiezoelectricity, by introducing a thermal field vector, and obtained the consistently, both mathematically and physically, the universal gradient equations in thermopiezoelectricity.

The aim of this research is to study the static and active vibration control of piezothermoelastic composite beam. The finite element model of piezothermoelastic composite beam is derived. The formulations are based on a high-order displacement field, a new high-order electrical potential field and a linear temperature model. In the present work, the constant-gain negative velocity feedback control scheme is used to active vibration control for piezolaminated beam, subjected to thermal excitation. The pyroelectric effect of the piezoelectric sensors/actuator due to the temperature variation of the environment is considered also. Specifically, the content of the paper is stated as follows. In Section 2, the fundamental equations of piezothermoelastic are summarized. The high-order displacement field and a new high-order electric potential model are developed in Section 3. Section 4 presents the finite element formulations. The numerical examples, including the PVDF bimorph and the piezothermoelastic behavior of composite beam, are considered in Section 5. In Section 6, some conclusions are indicated.

2. Fundamental piezothermoelastic linear equations

This section outlines the governing equations for piezothermoelastic materials. On account of the classical electromagnetic field and thermoelastic theories, the three-dimensional (3D) linear fundamental equations for a piezothermoelastic body of volume Ω can be summarized as follows (Altay and Dökmeci [19]).

2.1. Divergence equations

These equations relate to the linear stress equations of motion, the linear charge equations of electrostatics and the thermal energy balance equation

$$\begin{aligned} \sigma_{ij,j} + f_{bi} &= \rho\ddot{u}_i \quad \text{in } \Omega, \\ D_{i,i} - q &= 0 \quad \text{in } \Omega, \\ h_{i,i} - s &= -\theta_0\dot{\eta} \quad \text{in } \Omega, \end{aligned} \tag{1}$$

where σ_{ij} stand for the symmetric Cauchy stress tensor components, D_i for the electric displacement vector components, h_i for the components of heat flux vector, η, θ_0 are the entropy density and the constant positive reference temperature, respectively, f_i, q and s are body mechanical forces, electric charge and heat source in Ω, respectively. Note that standard tensors notation is used with Latin indices running from 1 to 3. They obey to Einstein's summation convention when repeated.

2.2. Gradient equations

The gradient equations correspond to the linear strain–mechanical displacement, linear electric field–electric potential and linear thermal field–temperature change relations. They state as

$$\begin{aligned} \varepsilon_{ij} &= \tfrac{1}{2}(u_{i,j} + u_{j,i}) \quad \text{in } \Omega, \\ E_i &= -\phi_{,i} \quad \text{in } \Omega, \\ h_i &= -\kappa_{ij}\theta_{,j} \quad \text{in } \Omega, \end{aligned} \tag{2}$$

where ε_{kl}, E_i, κ_{ij}, ϕ, θ are, respectively, the components of the symmetric Lagrange strain tensor, quasi-static electric field vector, conductivity tensor, electric potential, and temperature change from the reference one θ_0.

2.3. Constitutive equations

The linear constitutive equations coupling the piezothermoelastic field are given by (Benjeddou and Andrianarison [20])

$$\begin{aligned} \sigma_{ij} &= c_{ijkl}\varepsilon_{kl} - e_{kij}E_k - \lambda_{ij}\theta \quad \text{in } \Omega, \\ D_i &= e_{ijk}\varepsilon_{jk} + \chi_{ij}E_j + p_i\theta \quad \text{in } \Omega, \\ \eta &= \lambda_{ij}\varepsilon_{ij} + p_iE_i + \alpha\theta \quad \text{in } \Omega, \end{aligned} \tag{3}$$

where c_{ijkl}, e_{ijk}, χ_{ij} are the elastic, piezoelectric-stress and dielectric material constants, whereas p_i, λ_{ij} are pyroelectric and thermal stress–temperature material constants. α is a material constant given by

$$\alpha = \rho c_v \theta_0^{-1} \tag{4}$$

in which ρ is the mass density and c_v the specific heat under constant volume.

2.4. Boundary conditions

The regular boundary $\partial\Omega = S$ can be loaded with mechanical surface forces F_i on S_F, electric surface charge Q on S_Q, and a heat flux H on S_H. It can also support imposed mechanical displacements $\bar{u}_i$ on S_u,

an electric potential $\bar{\phi}$ on S_ϕ, a temperature $\bar{\theta}$ on S_θ. Where $S_F \cup S_u = S_q \cup S_\phi = S_h \cup S_\theta = S$ and $S_F \cap S_u = S_q \cap S_\phi = S_h \cap S_\theta = \varnothing$. The mechanical, electric and thermal boundary conditions can be written as

$$\begin{aligned} u_i &= \bar{u}_i \quad \text{on } S_u \quad \sigma_{ij} n_j = F \quad \text{on } S_F, \\ \phi &= \bar{\phi} \quad \text{on } S_\phi \quad D_i n_i = -Q \quad \text{on } S_Q, \\ \theta &= \bar{\theta} \quad \text{on } S_\theta \quad h_i n_i = H \quad \text{on } S_H. \end{aligned} \tag{5}$$

Eqs. (1)–(5) constitute the basic governing equations of linear piezothermoelasticty. After substituting Eqs. (2c) and (3c) into (1c), we get

$$\kappa_{ij}\theta_{,ij} = \theta_0(\lambda_{ij}\dot{\varepsilon}_{ij} + p_i\dot{E}_i + \alpha\dot{\theta}) \tag{6}$$

in which the heat source s is neglected. We can see that all equations of (1) are coupled. However, it is assumed in this paper that the dynamic couplings between the temperature and the mechanical and electric displacements are small. This assumption essentially provides that temperature changes due to changes in strains and electric fields are small compared with the magnitude of the thermal. Thus, temperature changes only produce mechanical and electrical forcing on the piezoelectric material. As a result, Eq. (6) reduces to

$$\kappa_{ij}\theta_{,ij} = \theta_0\alpha\dot{\theta}. \tag{7}$$

Therefore, we can firstly solve the uncoupled Eq. (7) and then study the coupled Eqs. (1a) and (1b) with the temperature treated as thermal load. In this paper, Eq. (7) is not considered presently, and the temperature in Eqs. (1a) and (1b) is assumed to be a prescribed value, i.e. a linear distribution along the axis 3 and independent of the x.

2.5. Generalized virtual work principle

For arbitrary space variable and admissible virtual displacement δu_i and potential $\delta\phi$, Eqs. (1a) and (1b) are equivalent to

$$\int_\Omega (\sigma_{ij,j} + f_{bi} - \rho\ddot{u}_i)\delta u_i \,\mathrm{d}\Omega + \int_\Omega (D_{i,i} - q)\delta\phi \,\mathrm{d}\Omega = 0. \tag{8}$$

Integrating by parts, this equation, and using the divergence theorem, leads to

$$\begin{aligned} &-\int_\Omega \sigma_{ij}\delta\varepsilon_{ij}\,\mathrm{d}\Omega - \int_\Omega \rho\ddot{u}_i\delta u_i\,\mathrm{d}\Omega + \int_\Omega D_i\delta E_i\,\mathrm{d}\Omega \\ &\int_\Omega f_{bi}\delta u_i\,\mathrm{d}\Omega - \int_\Omega q\delta\phi\,\mathrm{d}\Omega + \int_S \sigma_{ij}n_j\delta u_i\,\mathrm{d}S + \int_S D_i n_i\delta\phi\,\mathrm{d}S = 0. \end{aligned} \tag{9}$$

Using the symmetry property of the stress tensor, the boundary conditions (5) and the electric field–electric potential relation give

$$\begin{aligned} &-\int_\Omega \sigma_{ij}\delta\varepsilon_{ij}\,\mathrm{d}\Omega + \int_{S_F} F_i\delta u_i\,\mathrm{d}S + \int_\Omega f_{bi}\delta u_i\,\mathrm{d}\Omega + f_{ci}\delta u_i - \int_\Omega \rho\ddot{u}_i\delta u_i\,\mathrm{d}\Omega \\ &+ \int_\Omega D_i\delta E_i\,\mathrm{d}\Omega - \int_\Omega q\delta\phi\,\mathrm{d}\Omega - \int_{S_Q} Q\delta\phi\,\mathrm{d}S = 0, \end{aligned} \tag{10}$$

where f_{ci} is the components of concentrated load.

3. Mathematical formulation

3.1. Displacement and strain fields

The third-order displacement field used in this model is given by [21]

$$U(x,z,t) = u(x,t) - z\frac{\mathrm{d}w(x)}{\mathrm{d}x} + \left(z - z^3\frac{4}{3h^2}\right)\psi_x(x,t),$$
$$W(x,z,t) = w(x,t). \tag{11}$$

The x-axis is along the horizontal, z-axis is the vertical axis and this model is independent of the y-variable points 'into the page'. The functions $U(x,z,t)$ and $W(x,z,t)$ represent the horizontal and vertical displacements, respectively; there is no into-the-page displacement. The total thickness of the composite structure is h. The height of the top and bottom surface are $z = h/2$ and $z = -h/2$, respectively. The subfunctions $u(x,t)$ and $w(x,t)$ can be regarded as the mid-plane horizontal displacement and the mid-plane vertical displacement, respectively, while $\psi_x(x,t)$ is the shear rotation. Transverse normal strain is assumed to be negligible.

The set of strain equations can be derived from Eq. (11) using the usual definitions for strain (see Eq. (2a)), which become

$$\varepsilon_1 = \varepsilon_x = \frac{\mathrm{d}u}{\mathrm{d}x} - z\frac{\mathrm{d}^2w}{\mathrm{d}x^2} + \left(z - \frac{4z^3}{3h^2}\right)\frac{\mathrm{d}\psi_x}{\mathrm{d}x},$$
$$\varepsilon_5 = \gamma_{zx} = \psi_x\left(1 - \frac{4z^2}{h^2}\right). \tag{12}$$

In preparation for finite element implementation, the strain and displacement equations (12) and (11) can be expressed in a more convenient form as

$$\boldsymbol{u} = \boldsymbol{A}_u\boldsymbol{u}_u, \quad \boldsymbol{\varepsilon} = \boldsymbol{L}_u\boldsymbol{u}_u, \tag{13}$$

where $\boldsymbol{u} = [\,U \quad W\,]^{\mathrm{T}}$, $\boldsymbol{u}_u = [\,u \quad w \quad \psi_x\,]^{\mathrm{T}}$, $\boldsymbol{\varepsilon} = [\,\varepsilon_1 \quad \varepsilon_5\,]^{\mathrm{T}}$, and

$$A_u = \begin{bmatrix} 1 & -z\dfrac{\mathrm{d}}{\mathrm{d}x} & z - \dfrac{4z^3}{3h^2} \\ 0 & 1 & 0 \end{bmatrix}, \quad L_u = \begin{bmatrix} \dfrac{\mathrm{d}}{\mathrm{d}x} & -z\dfrac{\mathrm{d}^2}{\mathrm{d}x^2} & z - \dfrac{4z^3}{3h^2} \\ 0 & 0 & 1 - \dfrac{4z^2}{h^2} \end{bmatrix}.$$

Remarks: Many two-dimensional in-plane elements are usually based on low-order theory suitable for **thin** structures. The present element based upon the high-order displacement theory is applicable to both thin and moderately thick situations, and is able to account for the transverse shear effects in **thick** composites without the need for any shear correction factors.

3.2. High-order electric potential field

Bisegna and Maceri [22] pointed out that the electric potential distribution along the thickness of a piezoelectric layer has a quadratic component and this higher-order electric behavior should be addressed. This quadratic electric potential variation is directly coupled to the flexure of the actuators and its effect is of the same order as the bending stiffness of the actuators (Yang [23]). Although negligible for thin actuators, this effect should be included for thick actuators. To account for the quadratic electric potential distribution, the cubic function for electric potential was derived from the Hermitian shape function of beam element. The electric potential distribution along the thickness has an analogy to the deflection distribution along the x-axis, the electric field has an analogy to the shear rotation corresponding. Accordingly, the shape function for two-node Hermitian beam element was adopted to describe the electric potential distribution.

The electric potential inside the kth piezoelectric layer is considered through-thickness cubic, and written in the form

$$\phi^k(x,y,\tilde{z}) = f_1^k(\tilde{z})E_t^k(x,y) + f_2^k(\tilde{z})E_b^k(x,y) + f_3^k(\tilde{z})\bar{\phi}^k(x,y), \tag{14}$$

where $E_t^k(x,y)$ and $E_b^k(x,y)$ denote the electric field at the top and bottom surface, respectively, $\bar{\phi}^k(x,y)$ is the difference of electric potential between the top and bottom surface. The interpolation functions $f_i^k (i = 1,2,3)$ are

$$\left.\begin{aligned} f_1^k &= -\left(\tilde{z}+\tfrac{1}{2}\right)^2\left(\tilde{z}-\tfrac{1}{2}\right)h_k \\ f_2^k &= -\left(\tilde{z}+\tfrac{1}{2}\right)\left(\tilde{z}-\tfrac{1}{2}\right)^2 h_k \\ f_3^k &= 3\left(\tilde{z}+\tfrac{1}{2}\right)^2 - 2\left(\tilde{z}+\tfrac{1}{2}\right)^3 - \tfrac{1}{2} \end{aligned}\right\} \tag{15}$$

in which h_k is the thickness of the kth piezoelectric layer and $\tilde{z}$ is the local thickness coordinate of the kth piezoelectric layer, $\tilde{z} \in [-1/2 \quad 1/2]$ given by

$$\tilde{z} = \frac{z}{h_k} - \frac{z_t^k + z_b^k}{2h_k}, \tag{16}$$

where z_t^k and z_b^k are the z-axis coordinates for the top and bottom surfaces of the kth piezoelectric layer, respectively.

It can be noted that there are two special advantages of this electric potential field:

(i) The boundary condition of applied voltages ($\bar{\phi}^k$), the major electrical boundary condition, is satisfied accurately as follows:

$$\phi^k(x,y,\tilde{z})\big|^{z=z_t^k} - \phi^k(x,y,\tilde{z})\big|^{z=z_b^k} = \bar{\phi}^k. \tag{17}$$

(ii) It is convenient to deal with the conjuncture conditions between two piezoelectric layers by using of the electric field at the interface. For more accurately modelling of electric potential, this model may extend to layerwise cubic electric potential approximations conveniently.

Using the usual definition of the electric field being the negative gradient of the electric potential, the electric field has the following expression:

$$\boldsymbol{E}_k = \begin{bmatrix} E_x \\ E_z \end{bmatrix}_k = \begin{Bmatrix} -\dfrac{\partial\phi}{\partial x} \\ -\dfrac{\partial\phi}{\partial z} \end{Bmatrix}_k = -\begin{bmatrix} f_1^k\dfrac{\mathrm{d}}{\mathrm{d}x} & f_2^k\dfrac{\mathrm{d}}{\mathrm{d}x} & f_3^k\dfrac{\mathrm{d}}{\mathrm{d}x} \\ \dfrac{\mathrm{d}f_1^k}{\mathrm{d}z} & \dfrac{\mathrm{d}f_2^k}{\mathrm{d}z} & \dfrac{\mathrm{d}f_3^k}{\mathrm{d}z} \end{bmatrix} \begin{Bmatrix} E_t^k \\ E_b^k \\ \bar{\phi}^k \end{Bmatrix} = -\boldsymbol{L}_\phi^k \boldsymbol{u}_\phi^k. \tag{18}$$

Note that because the electric potential is chosen to be independent of the y-dimension, by definition the electric field $E_y = 0$.

3.3. Linear temperature field

The expression for the temperature field (θ) is assumed as a linear function of the thickness of the beam:

$$\theta(x,z) = \left(\frac{1}{2} - \frac{z}{h}\right)\theta_b(x) + \left(\frac{1}{2} + \frac{z}{h}\right)\theta_t(x) = \boldsymbol{B}_\theta\boldsymbol{\theta}, \tag{19}$$

where θ_t, θ_b are the top ($z/h = 1/2$) and bottom ($z/h = -1/2$) surface temperature, respectively. $\boldsymbol{B}_\theta = [1/2 - z/h \quad 1/2 + z/h]$ is the linear interpolation vector for the temperature variation through the depth; $\boldsymbol{\theta} = [\theta_b \quad \theta_t]^{\mathrm{T}}$ is the vector of surface temperatures.

4. Finite element formulation

The analytical formulation described above is complete and solutions can be obtains from it. An exact solution may be adopted to solve a particular problem or a finite element approach may be used to solve a more general problem. For the finite element formulation, the degrees of freedom consist of the mechanical variables, electric potential, and temperature variables. At this point, the finite element work will use a two nodes Hermitian beam element. The goal of the following derivations is to express the strain–displacement, electric field–electric potential relations using nodal values and shape functions and then to use this in the integrand of the generalized virtual work formulation.

4.1. Hermitian beam element

The mechanical variable equation (11) that is based on the third-order displacement theory will be converted to its finite element representation using appropriate shape functions and mechanical nodal variables. The mechanical element being considered is a 1D Hermitian beam element for transverse displacements, as shown in Fig. 1. The three mechanical variables $\boldsymbol{u}_u$ will be expressed using four mechanical nodal variables $\boldsymbol{u}_u^e$ as follows:

$$\boldsymbol{u}_u = \boldsymbol{N}_u \boldsymbol{u}_u^e, \tag{20}$$

where $\boldsymbol{u}_u^e = \{u_1, w_1, \psi_{x1}, (\mathrm{d}w/\mathrm{d}x)_1, u_2, w_2, \psi_{x2}, (\mathrm{d}w/\mathrm{d}x)_2\}^{\mathrm{T}}$, shape function matrix

$$\boldsymbol{N}_u = \begin{bmatrix} N_1^0 & 0 & 0 & 0 & N_2^0 & 0 & 0 & 0 \\ 0 & N_1 & 0 & N_1'(l_e/2) & 0 & N_2 & 0 & N_2'(l_e/2) \\ 0 & 0 & N_1^0 & 0 & 0 & 0 & N_2^0 & 0 \end{bmatrix}$$

in which N_1^0, N_2^0 are the Lagrangian shape functions defined as

$$N_1^0 = N_1^0(\xi) = (1-\xi)/2, \quad N_2^0 = N_2^0(\xi) = (1+\xi)/2 \tag{21}$$

and the Hermitian shape functions are

$$\begin{aligned} N_1 &= N_1(\xi) = \tfrac{1}{4}(1-\xi)^2(2+\xi), \quad N_2 = N_2(\xi) = \tfrac{1}{4}(2-\xi)(1+\xi)^2, \\ N_1' &= N_1'(\xi) = \tfrac{1}{4}(1-\xi)^2(1+\xi), \quad N_2' = N_2'(\xi) = -\tfrac{1}{4}(1-\xi)(1+\xi)^2, \end{aligned} \tag{22}$$

where ξ is the local coordinate defined as

$$\xi = 2\frac{x - x_1}{x_2 - x_1} - 1.$$

Using Eqs. (20) and (13), the displacements vector and the strain vector can be expressed as follows:

$$\begin{aligned} \boldsymbol{u} &= \boldsymbol{A}_u \boldsymbol{u}_u = \boldsymbol{A}_u \boldsymbol{N}_u \boldsymbol{u}_u^e = \boldsymbol{N} \boldsymbol{u}_u^e, \\ \varepsilon &= \boldsymbol{L}_u \boldsymbol{u}_u = \boldsymbol{L}_u \boldsymbol{N}_u \boldsymbol{u}_u^e = \boldsymbol{B}_u \boldsymbol{u}_u^e, \end{aligned} \tag{23}$$

where the $\boldsymbol{N}$, $\boldsymbol{B}_u$ are, respectively, the displacement interpolation matrix, strain interpolation matrix.

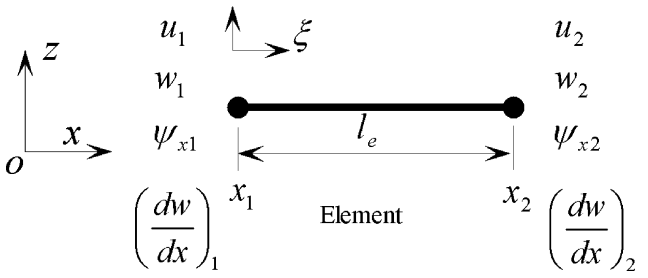

Fig. 1. Two-node beam element and local coordinate system.

Again, using linear Lagrangian interpolation functions for E_t, E_b, and $\bar{\phi}$, the vector $\boldsymbol{u}_\phi$ is expressed as

$$\boldsymbol{u}_\phi = \boldsymbol{N}_\phi \boldsymbol{u}_\phi^e, \tag{24}$$

where

$$\boldsymbol{N}_\phi = [\, N_1^0 \boldsymbol{I}_3 \quad N_2^0 \boldsymbol{I}_3 \,] \quad \text{and} \quad \boldsymbol{u}_\phi^e = [\, E_t^1 \quad E_b^1 \quad \bar{\phi}^1 \quad E_t^2 \quad E_b^2 \quad \bar{\phi}^2 \,]^{\mathrm{T}}$$

in which $\boldsymbol{I}_3$ is the 3×3 identity matrix.

From Eqs. (18) and (24), the electric field $\boldsymbol{E}$ is expressed as

$$\boldsymbol{E} = -\boldsymbol{L}_\phi \boldsymbol{u}_\phi = -\boldsymbol{L}_\phi \boldsymbol{N}_\phi \boldsymbol{u}_\phi^e = -\boldsymbol{B}_\phi \boldsymbol{u}_\phi^e. \tag{25}$$

Rewrite Eqs. (3a) and (3b) in vector form, they are

$$\begin{aligned} \boldsymbol{\sigma} &= \boldsymbol{C}\boldsymbol{\varepsilon} - \boldsymbol{e}^{\mathrm{T}}\boldsymbol{E} - \boldsymbol{\lambda}\boldsymbol{\theta}, \\ \boldsymbol{D} &= \boldsymbol{e}\boldsymbol{\varepsilon} + \boldsymbol{\chi}\boldsymbol{E} + \boldsymbol{p}\boldsymbol{\theta}, \end{aligned} \tag{26}$$

where $\boldsymbol{\sigma}$ and $\boldsymbol{D}$ are the stress vector and the electric displacement vector, respectively. $\boldsymbol{\varepsilon}$ and $\boldsymbol{E}$ are the strain vector and the electric field vector, respectively. Matrices $\boldsymbol{C}$, $\boldsymbol{\chi}$, $\boldsymbol{e}$, $\boldsymbol{\lambda}$ and $\boldsymbol{p}$ are the matrix forms of elastic constant, dielectric permittivity, piezoelectric constant, thermal–mechanical coupling constant (thermal stress coefficient), and thermal–piezoelectric coupling constant (pyroelectric constant), respectively.

4.2. Dynamic equations

Substituting Eqs. (23)–(26) into Eq. (10) and assembling the element equations yields

$$\begin{aligned} &\boldsymbol{M}\ddot{\boldsymbol{u}}_u + \boldsymbol{K}_{uu}\boldsymbol{u}_u + \boldsymbol{K}_{ua}\boldsymbol{u}_a + \boldsymbol{K}_{us}\boldsymbol{u}_s = \boldsymbol{F}_u + \boldsymbol{K}_{u\theta}\boldsymbol{\theta}, \\ &\boldsymbol{K}_{au}\boldsymbol{u}_u - \boldsymbol{K}_{aa}\boldsymbol{u}_a = -\boldsymbol{F}_a - \boldsymbol{K}_{a\theta}\boldsymbol{\theta}, \\ &\boldsymbol{K}_{su}\boldsymbol{u}_u - \boldsymbol{K}_{ss}\boldsymbol{u}_s = -\boldsymbol{F}_s - \boldsymbol{K}_{s\theta}\boldsymbol{\theta}. \end{aligned} \tag{27}$$

Note that the piezoelectric layers include the piezoelectric sensor and actuator layers, thus, the vector $\boldsymbol{u}_\phi$ is partitioned to actuator vector $\boldsymbol{u}_a$ and sensor vector $\boldsymbol{u}_s$. The subscript a and s denote the actuator and sensor, respectively. The matrices and vectors are given by the mass matrix $\boldsymbol{M} = \int_V \rho \boldsymbol{N}^{\mathrm{T}}\boldsymbol{N}\,\mathrm{d}V$, the elastic matrix $\boldsymbol{K}_{uu} = \int_V \boldsymbol{B}_u^{\mathrm{T}}\boldsymbol{C}\boldsymbol{B}_u\,\mathrm{d}V$, matrix coupling thermal–mechanical $\boldsymbol{K}_{u\theta} = \int_V \boldsymbol{B}_u^{\mathrm{T}}\boldsymbol{\lambda}\boldsymbol{B}_\theta\,\mathrm{d}V$, matrix coupling electric-mechanical for actuator and sensor $\boldsymbol{K}_{ui} = \int_{V_i} \boldsymbol{B}_u^{\mathrm{T}}\boldsymbol{e}^{\mathrm{T}}\boldsymbol{B}_\phi\,\mathrm{d}V$ $(i = a, s)$, the permittivity matrix for actuator and sensor $\boldsymbol{K}_{kk} = \int_{V_k} \boldsymbol{B}_\phi^{\mathrm{T}}\boldsymbol{\chi}_k\boldsymbol{B}_\phi\,\mathrm{d}V$ $(k = s, a)$, the matrix coupling electric–thermal for actuator and sensor $\boldsymbol{K}_{k\theta} = \int_{V_k} \boldsymbol{B}_\phi^{\mathrm{T}}\boldsymbol{p}_k\boldsymbol{B}_\theta\,\mathrm{d}V$ $(k = s, a)$, the mechanical load vector $\boldsymbol{F}_u = \int_V \boldsymbol{N}^{\mathrm{T}}\boldsymbol{f}_b\,\mathrm{d}V + \int_{S_F} \boldsymbol{N}^{\mathrm{T}}\boldsymbol{F}\,\mathrm{d}S + \boldsymbol{N}^{\mathrm{T}}\boldsymbol{f}_c$, the applied charge vector $\boldsymbol{F}_k = \int_{S_D} \boldsymbol{N}_\phi^{\mathrm{T}}\boldsymbol{f}_k^{\mathrm{T}}Q\,\mathrm{d}S$ $(k = s, a)$.

Eq. (27) shows the coupling of the displacement and electric fields. It should be noted that the material properties are dependent on their positions. As a stress free reference temperature $\theta_0 = 0\,^{\circ}\mathrm{C}$ is assumed, the temperature field is not coupled with the structure deflection and electric field. Consequently, the temperature field is assumed to vary in the thickness direction only as mentioned above.

4.3. Reduction for degree of freedoms

Note that the electric variables include the electric-field variables and the electric-potential variables. In general, we concern the electric-potential variables only. Suppose that the total electric variables of the full model are divided into the electric-field degree of freedoms $\boldsymbol{\delta}_{aE}$, $\boldsymbol{\delta}_{sE}$ and the electric-potential degree of freedoms $\boldsymbol{\delta}_{a\phi}$, $\boldsymbol{\delta}_{s\phi}$, corresponding to this partition, the dynamic equation (27) follows

$$\begin{aligned} &\boldsymbol{M}\ddot{\boldsymbol{u}}_u + \boldsymbol{K}_{uu}\boldsymbol{u}_u + \boldsymbol{K}_{auE}\boldsymbol{\delta}_{aE} + \boldsymbol{K}_{au\phi}\boldsymbol{\delta}_{a\phi} + \boldsymbol{K}_{suE}\boldsymbol{\delta}_{sE} + \boldsymbol{K}_{su\phi}\boldsymbol{\delta}_{s\phi} = \boldsymbol{F}_u + \boldsymbol{K}_{u\theta}\boldsymbol{\theta}, \\ &\boldsymbol{K}_{aEu}\boldsymbol{u}_u - \boldsymbol{K}_{aEE}\boldsymbol{\delta}_{aE} - \boldsymbol{K}_{aE\phi}\boldsymbol{\delta}_{a\phi} = -\boldsymbol{F}_{aE} - \boldsymbol{K}_{aE\theta}\boldsymbol{\theta}, \end{aligned}$$

$$\begin{aligned}
&\boldsymbol{K}_{a\phi u}\boldsymbol{u}_u - \boldsymbol{K}_{a\phi E}\boldsymbol{\delta}_{aE} - \boldsymbol{K}_{a\phi\phi}\boldsymbol{\delta}_{a\phi} = -\boldsymbol{F}_{a\phi} - \boldsymbol{K}_{a\phi\theta}\boldsymbol{\theta},\\
&\boldsymbol{K}_{sEu}\boldsymbol{u}_u - \boldsymbol{K}_{sEE}\boldsymbol{\delta}_{sE} - \boldsymbol{K}_{sE\phi}\boldsymbol{\delta}_{s\phi} = -\boldsymbol{F}_{sE} - \boldsymbol{K}_{sE\theta}\boldsymbol{\theta},\\
&\boldsymbol{K}_{s\phi u}\boldsymbol{u}_u - \boldsymbol{K}_{s\phi E}\boldsymbol{\delta}_{sE} - \boldsymbol{K}_{s\phi\phi}\boldsymbol{\delta}_{s\phi} = -\boldsymbol{F}_{s\phi} - \boldsymbol{K}_{s\phi\theta}\boldsymbol{\theta}.
\end{aligned} \tag{28}$$

From Eqs. (28b) and (28d), the electric-field degree of freedoms are expressed as

$$\begin{aligned}
\boldsymbol{\delta}_{aE} &= \boldsymbol{K}_{aEE}^{-1}\boldsymbol{K}_{aEu}\boldsymbol{u}_u - \boldsymbol{K}_{aEE}^{-1}\boldsymbol{K}_{aE\phi}\boldsymbol{\delta}_{a\phi} + \boldsymbol{K}_{aEE}^{-1}\boldsymbol{K}_{aE\theta}\boldsymbol{\theta},\\
\boldsymbol{\delta}_{sE} &= \boldsymbol{K}_{sEE}^{-1}\boldsymbol{K}_{sEu}\boldsymbol{u}_u - \boldsymbol{K}_{sEE}^{-1}\boldsymbol{K}_{sE\phi}\boldsymbol{\delta}_{s\phi} + \boldsymbol{K}_{sEE}^{-1}\boldsymbol{K}_{sE\theta}\boldsymbol{\theta}.
\end{aligned} \tag{29}$$

It should be noted that the interpolation $f_{1k} = f_{2k} = 0$ $(k = s, a)$ on the top and bottom surfaces of sensor and actuator layer. Substituting Eq. (29) into the other three equations of (28), we can obtain

$$\begin{aligned}
&\boldsymbol{M}\ddot{\boldsymbol{u}}_u + \bar{\boldsymbol{K}}_{uu}\boldsymbol{u}_u + \bar{\boldsymbol{K}}_{ua}\boldsymbol{u}_a + \bar{\boldsymbol{K}}_{us}\boldsymbol{u}_s = \boldsymbol{F}_u + \bar{\boldsymbol{K}}_{u\theta}\boldsymbol{\theta},\\
&\bar{\boldsymbol{K}}_{au}\boldsymbol{u}_u - \bar{\boldsymbol{K}}_{aa}\boldsymbol{\delta}_{a\phi} = -\boldsymbol{F}_{a\phi} - \bar{\boldsymbol{K}}_{a\theta}\boldsymbol{\theta},\\
&\bar{\boldsymbol{K}}_{su}\boldsymbol{u}_u - \bar{\boldsymbol{K}}_{ss}\boldsymbol{\delta}_{s\phi} = -\boldsymbol{F}_{s\phi} - \bar{\boldsymbol{K}}_{s\theta}\boldsymbol{\theta}.
\end{aligned} \tag{30}$$

Furthermore, the displacement and electric potential equations can be decoupled using Guyan's reduction scheme (Tzou and Tseng [6]). Substituting Eqs. (30b) and (30c) into Eq. (30a), we obtain

$$\boldsymbol{M}\ddot{\boldsymbol{u}}_u + \boldsymbol{C}\dot{\boldsymbol{u}}_u + \boldsymbol{K}\boldsymbol{u}_u = \boldsymbol{F}_u + \boldsymbol{F}_\theta + \boldsymbol{F}_\phi, \tag{31}$$

where the global stiffness matrix $\bar{\boldsymbol{K}} = \bar{\boldsymbol{K}}_{uu} + \bar{\boldsymbol{K}}_{ua}\bar{\boldsymbol{K}}_{aa}^{-1}\bar{\boldsymbol{K}}_{au} + \bar{\boldsymbol{K}}_{us}\bar{\boldsymbol{K}}_{ss}^{-1}\bar{\boldsymbol{K}}_{su}$, and the thermal vectors due to the thermal strain effect and pyroelectric effect $\boldsymbol{F}_\theta = (\bar{\boldsymbol{K}}_{u\theta} - \bar{\boldsymbol{K}}_{ua}\bar{\boldsymbol{K}}_{aa}^{-1}\bar{\boldsymbol{K}}_{a\theta} - \bar{\boldsymbol{K}}_{us}\bar{\boldsymbol{K}}_{ss}^{-1}\bar{\boldsymbol{K}}_{s\theta})\boldsymbol{\theta}$. The applied charge vector $\boldsymbol{F}_\phi = -\bar{\boldsymbol{K}}_{ua}\bar{\boldsymbol{K}}_{aa}^{-1}\boldsymbol{F}_{a\phi} - \bar{\boldsymbol{K}}_{us}\bar{\boldsymbol{K}}_{ss}^{-1}\boldsymbol{F}_{s\phi}$. The damping matrix $\boldsymbol{C} = \alpha\boldsymbol{M} + \beta\boldsymbol{K}$, in which α, β are Rayleigh's coefficients.

For the sensor layer, the applied charge is zero and the converse piezoelectric effect is assumed negligible. Using Eq. (28c), the sensor output is

$$\boldsymbol{\delta}_{s\phi} = \bar{\boldsymbol{K}}_{ss}^{-1}\bar{\boldsymbol{K}}_{su}\boldsymbol{u}_u + \bar{\boldsymbol{K}}_{ss}^{-1}\bar{\boldsymbol{K}}_{s\theta}\boldsymbol{\theta}. \tag{32}$$

The sensor output voltage can be feed back through an amplifier to the actuator with a change of polarity. In order to provide proper velocity information to the piezoelectric actuators, the voltage induced in the sensor is differentiated and feedback. Accordingly, a feedback control gain is used to enhance the sensor signal and also to change its sign before the voltage is injected into the piezoelectric actuators. In case of constant-gain velocity feedback control the electrical potential is to be fed back to the actuator is calculated as

$$\boldsymbol{\delta}_{a\phi} = -\boldsymbol{G}\dot{\boldsymbol{\delta}}_{s\phi}, \tag{33}$$

where $\boldsymbol{G}$ is the control gain.

In case of multiinput multioutput (MIMO) controllers, the actuator voltages and sensor voltages are vectors and the control gain is a matrix. However, in case of single input single output system, the actuator and sensor voltage become scalars and control gain becomes a single value. In case of MIMO control system, when there are large numbers of sensor/actuator patches with large variation in voltage range, implementation of the control strategy becomes practically difficult.

5. Example results and discussions

This section aims to validate the theoretical formulation of the present high-order model by comparing its numerical results with the experimental and numerical results of other researchers and to provide some new results. The following numerical experiments are divided into two categories:

(i) PVDF bimorph beam.
(ii) Piezothermoelastic behavior and control of a cantilever piezolaminated beam.

5.1. PVDF bimorph beam

To validate the model, a piezoelectric bimorph cantilever beam (Fig. 2, 100 mm × 5 mm × 1 mm) constructed of two PVDF bonded together with opposite polarities is considered. This particular example has been considered by the following researchers: Hwang and Park [24], Tzou and Ye [25], and Chee and Steven [21]. The relevant data for PVDF bimorph are shown in Table 1.

Case I (Actuator model): When a unit voltage is applied across the thickness, the induced internal stresses result in a bending moment, which causes bimorph beam to bend. The theoretical solution to the deflection of the beam is given by Smits [26]:

$$w(x) = \frac{3}{2}\frac{e_{31}V}{E}\left(\frac{x}{h}\right)^2, \tag{34}$$

where E is Young's modulus, V the applied voltage, and h the thickness of the beam.

The bimorph beam is modeled using five elements of equal length. The numerical results for the present method are compared with results from other methods in Table 2. Tzou and Ye [25], using triangular shell elements, which have both mechanical (FOSDT) and electrical dofs, showed that they produced better results

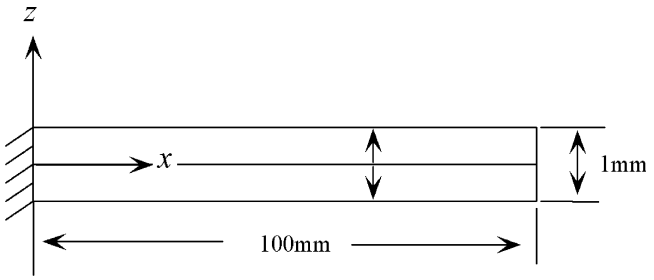

Fig. 2. PVDF bimorph cantilever beam.

Table 1
Properties for PVDF bimorph cantilever

Elastic modulus	2.0×10^9 Pa
Shear modulus	7.75×10^8 Pa
Mass density	1.8×10^3 kg m^{-3}
Poisson's ratio	0.29
e_{31} piezo	0.046 C m^{-2}
e_{32} piezo	0.046 C m^{-2}
Elec. perm. χ_{11}	1.06×10^{-10} F m^{-1}
Elec. perm. χ_{22}	1.06×10^{-10} F m^{-1}
Elec. perm. χ_{33}	1.06×10^{-10} F m^{-1}

Table 2
Deflections along length of beam ($\times 10^{-7}$ m)

$x(m)$	Theory—Smits	Solid FE—Tzou	Shell FE—Tzou/Ye	Mixed FE—Chee	Present
0.02	0.138	0.124	0.132	0.138	0.136
0.04	0.552	0.508	0.528	0.552	0.545
0.06	1.24	1.16	1.19	1.242	1.226
0.08	2.21	2.10	2.11	2.208	2.18
0.1	3.45	3.30	3.30	3.45	3.41
dof	–	96	132	42	42

than the thin solid linear elements used by Tzou. The results from the mixed finite element model (Chee et al. [21]), which uses the Hermitian beam elements with electric potential incorporated via the layerwise formulation, are fairly agree with theoretical analysis; however, the total number of degrees of freedom is higher due to the layerwise linear electric potential. The present model, which uses Hermitian beam elements with high-order electric potential distribution, has a high correlation with the theoretical solutions and a lower total number of degrees of freedom.

Case II (Sensor model): The second study was where the distributed voltage along the beam was calculated, when the tip of the beam has load. The bimorph beam is made to deflect to produce 10 mm tip deflection and the output voltage calculated is shown in Fig. 3. In the model of Hwang and Park there are five pieces of separate electrode, being an equipotential surface, must have a constant voltage, hence the step distribution in Fig. 3. However, in practice, it should be possible to have point electrodes located at positions of interest. So measuring the sensor voltages from these point electrodes would produce a sensor distribution as shown by the results of Tzou and Tseng [6] and the present model. Fig. 3 also indicates a good correlation between Tzou et al. and the present model.

Case III (Electric potential distribution along thickness): The third study considered the distributed voltage through thickness of the parallel piezoelectric (PVDF) bimorph with 1 mm tip deflection. The ANSYS coupled-field analysis program ANSYS Multi-physics is used to carry out a full 3D analysis by considering the coupled-field brick elements (Solid5) and the results from the full 3D FEM are taken as accurate in the present

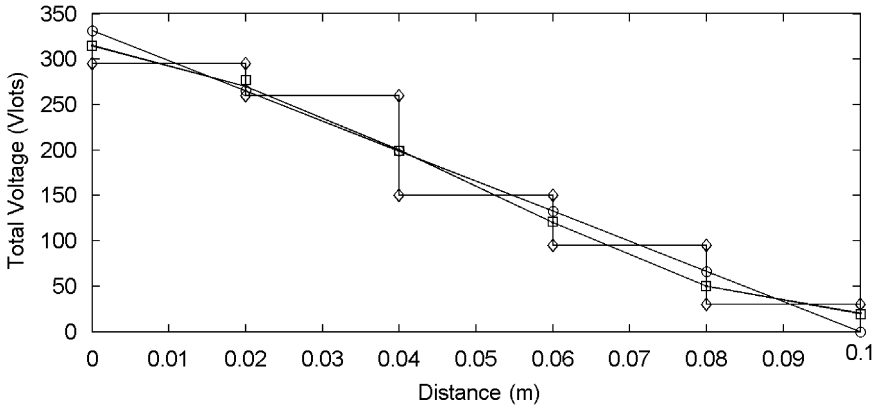

Fig. 3. The sensor voltage distribution for the bending actuation. (○ present; □ Tzou/Tseng; ◇ Hwang/Park.)

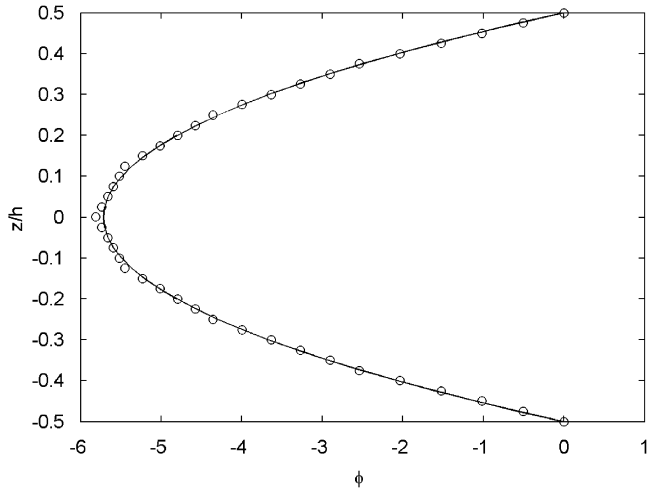

Fig. 4. Electric potential distribution along thickness (○ Ansys;-Present).

numerical comparison. Fig. 4 shows that the through-the-thickness variation of the electric potential ($x = l/2$) predicted by the present model can also be a good approximation to the nonlinear variation predicted by the full 3D model. Therefore, the present model can predict the actual through-the-thickness electric potential field. It can be observed that there is significant error in ϕ when the linear electric potential model is adopted, which will cause the induced potential of the piezoelectric sensors in closed circuit to vanish.

5.2. Piezothermoelastic behavior and control of a cantilever piezolaminated beam

Piezothermoelastic behavior and control of a cantilever piezolaminated graphite/epoxy beam has been studied. The piezolaminated model considered (Fig. 5, $L = 0.5\,\mathrm{m}$, $h_b = 0.01\,\mathrm{m}$, $b = 0.01\,\mathrm{m}$, and $h_p = 1 \times 10^{-3}\,\mathrm{m}$) is a graphite/epoxy beam sandwiched between two PZT layers. This beam has been modeled using the present piezolaminated beam element. Material properties are summarized in Table 3 in terms of reference material coefficient values: elastic modulus $E_0 = 2 \times 10^9\,\mathrm{N\,m^{-2}}$; Poisson's ratio $v_0 = 1/3$; thermal expansion $\alpha_0 = 1.2 \times 10^{-4}$; electric permittivity $\chi_0 = 1 \times 10^{-10}\,\mathrm{F\,m^{-1}}$; piezoelectric compliance $d_0 = 2.5 \times 10^{-11}\,\mathrm{C\,N^{-1}}$; and pyroelectric constant $p_0 = 2.5 \times 10^{-5}\,\mathrm{C\,K^{-1}\,m^{-2}}$. It is assumed that all the material properties are constant over the temperature range studied in this work.

Three cases were considered. In the first case, the piezothermoelastic effect (sensing capability) of the distributed piezoelectric sensor due to thermal excitation has been considered. The second case is examining the deflection due to the thermal gradient. The third case is to demonstrate a control method to simultaneously control the dynamic deflection and thermally induced static deflection.

Case 1 (Piezothermoelastic effect): Voltage generation in the PZT sensor due to elevated temperature field.

It has been assumed that the beam with the PZT sensor and actuator is placed in an elevated temperature field and the beam temperature quickly reaches a steady state. It is assumed that there is only one piece of electrode on the PZT layer. From Eq. (32), It can be noted that the temperature variation can induce an output voltage in the PZT sensor—***the pyroelectric effect.*** In addition, the thermally induced deformation can also induce a sensor signal. This piezothermoelastic effect has been studied and these two sensor or voltages

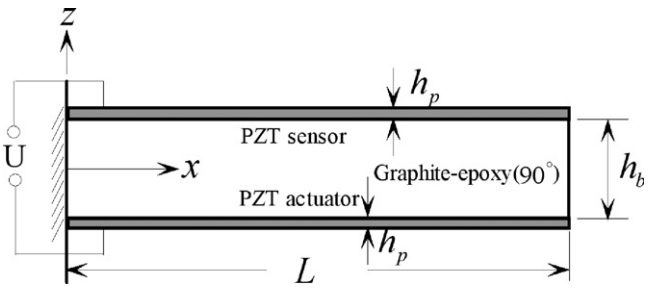

Fig. 5. Piezolaminated cantilever composite beam.

Table 3
Material properties from Blandford et al. [27]

Properties	PZT	Graphite–epoxy
Elastic modulus	$E_1 = E_2 = E_3 = 30E_0$	$E_1 = 90E_0$, $E_2 = E_3 = 5E_0$
Poisson's ratio	$v_{12} = v_{13} = v_{23} = v_0$	$v_{12} = v_{13} = v_{23} = v_0$
Shear modulus	$G_{12} = G_{13} = G_{23} = 11.25E_0$	$G_{12} = G_{13} = 4E_0$, $G_{23} = 1.5E_0$
Thermal expansion	$\alpha_1 = \alpha_2 = \alpha_3 = 0.01\alpha_0$	$\alpha_1 = 0.0002\alpha_0$, $\alpha_2 = \alpha_3 = 0.2\alpha_0$
Electric permittivity	$\chi_{11} = \chi_{22} = \chi_{33} = 150\chi_0$	–
Piezoelectric compliance	$d_{31} = d_{32} = -7d_0$, $d_{24} = d_{15} = 24d_0$, $d_{33} = 14d_0$	–
Pyroelectric constant	$p_3 = -p_0$	–
Mass density ($\mathrm{kg\,m^{-3}}$)	7750	1600

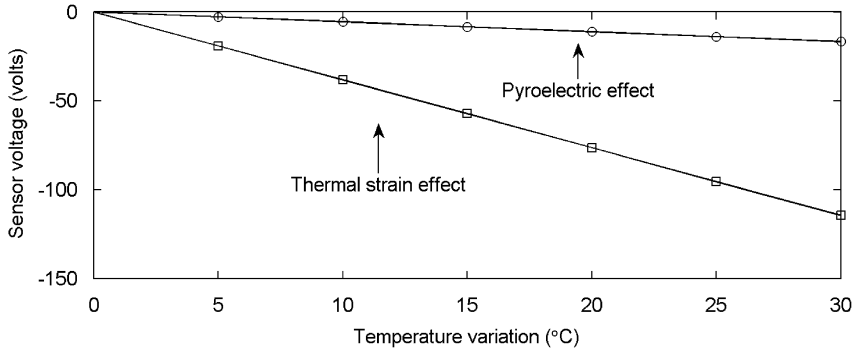

Fig. 6. Sensor voltage generated due to thermal excitation.

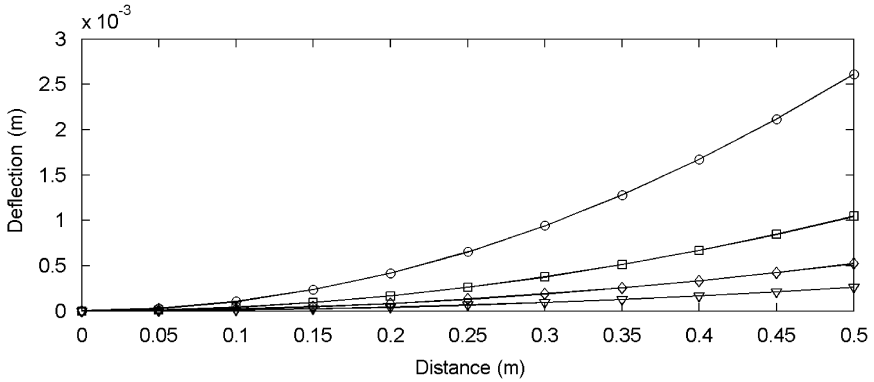

Fig. 7. Deflection due to thermal gradient (○ 50 °C; □ 20 °C; ◇ 10 °C; ▽ 5 °C).

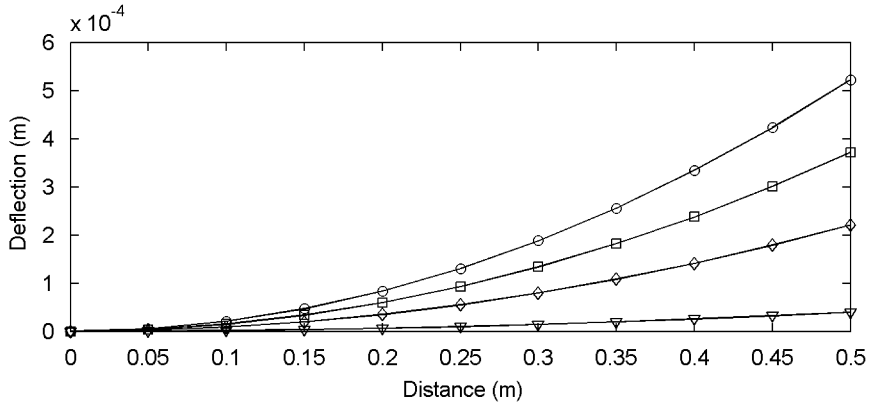

Fig. 8. Static control of the thermally induced static deflection for a thermal gradient of 10 °C (○ $\phi_a = 0$ V; □ $\phi_a = 50$ V; ◇ $\phi_a = 100$ V; ▽ $\phi_a = 160$ V).

are shown in Fig. 6. It can be noted that the thermal strain effect is more significant than the pyroelectric effect on the piezoelectric layers.

Case 2 (Theramlly induced deflection and control): In this case, a temperature gradient has been applied to the piezolaminated beam such that the temperature of the bottom surface is higher than the top surface. Owing to this temperature gradient the middle of the beam deflects upwards. Fig. 7 indicates the centerline deflection of the beam for 5, 10, 20, and 50 °C temperature gradients.

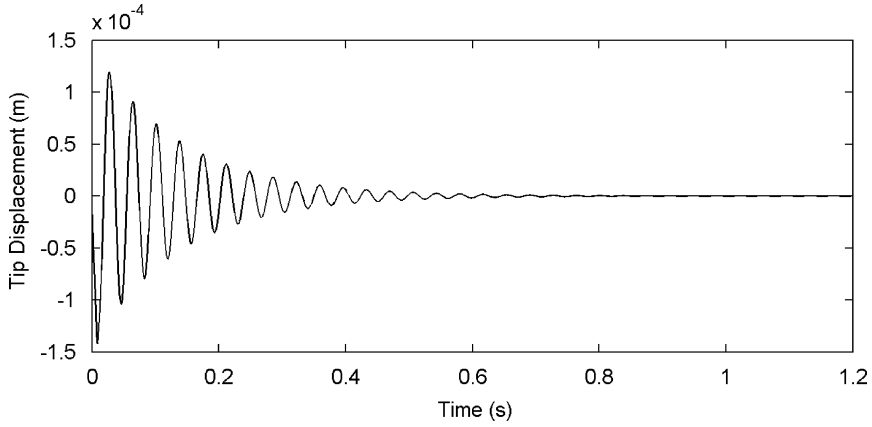

Fig. 9. Controlled dynamic response without thermal effect ($G = 0.02$).

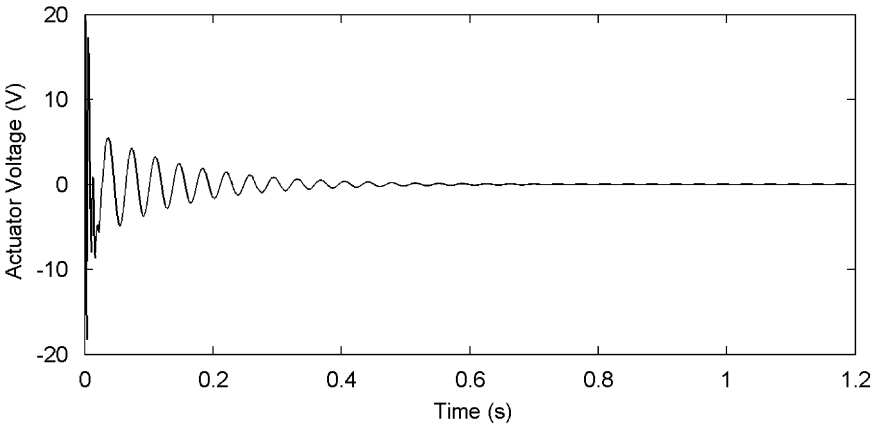

Fig. 10. Actuator voltage corresponding to Fig. 9.

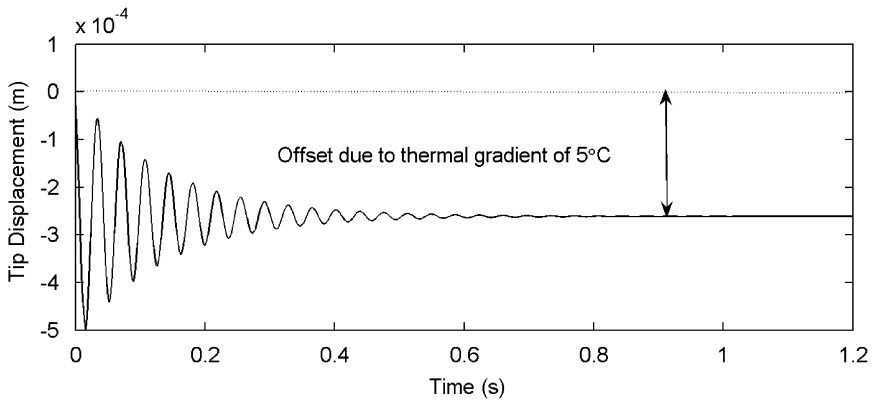

Fig. 11. Controlled dynamic response with a thermal gradient of 5 °C ($G = 0.02$).

Fig. 8 shows the reduction in the thermally induced static offset due to a static voltage applied to both the piezoelectric layers (sensor and actuator layers) and how the static deflection is gradually reduced with the increase of the static voltage. It can be noted that the static control voltages needed to compensate the thermally induced static deflection is quite high even for a small thermal gradient of 10 °C.

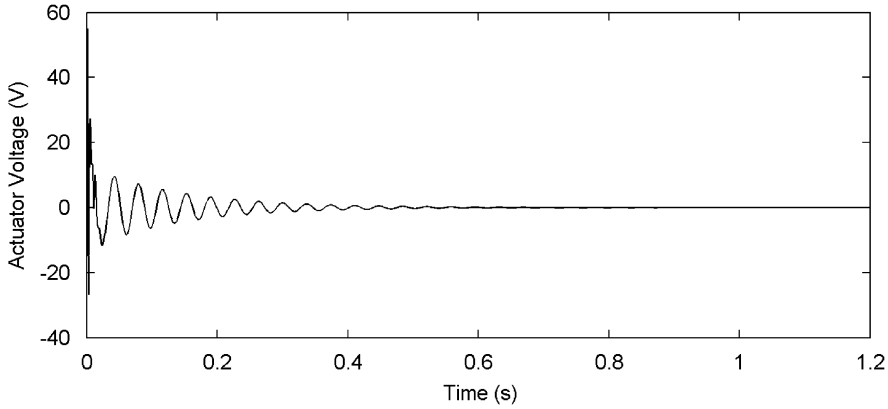

Fig. 12. Actuator voltage corresponding to Fig. 11.

Case 3 (Active vibration control with prescribed thermal gradient): An external impulse load of 1 N is assumed to act at the free end of the beam for 1 ms duration. Active vibration control performance has been studied using negative velocity feedback control scheme and a natural structural damping of 1% has been assumed. Figs. 9 and 10 show the controlled tip displacement versus time and actuator voltage versus time for the case where there is no thermal gradient. Figs. 11 and 12 indicate the controlled tip displacement and actuator voltage for the piezolaminated beam subjected to a thermal gradient of 5 °C when subjected to an external impulse load of 1 N. It can be noted from Fig. 11 that there is thermally induced offset, due to a temperature gradient of 5 °C in the controlled response. That is, the thermally induced offset is not controlled using the negative velocity feedback control scheme, which is only effective for the control of dynamic oscillation.

6. Conclusions

In the present paper, high-order shear deformable piezolaminated beam is formulated including the stiffness, mass and thermoelectromechanical coupling effects of distributed piezoelectric sensor and actuator layers. A new high-order electrical potential distributed model and a linear temperature field are used to derive the dynamic model. The active vibration control performance of a piezolaminated beam is studied using constant-gain negative velocity feedback control scheme.

A PVDF bimorph and a piezolaminated graphite–epoxy beam have been considered for case studies. The quadratic electric potential distribution along thickness is captured, which is good approximation to the nonlinear variation predicted by the full 3D model. It has been shown that the sensor voltage contributed by the thermal strain effect is much more than that contributed by pyroelectric effect. The thermally induced static deflection due to the thermal gradients between top and bottom surfaces of the beam has been studied. It has been shown that the thermal gradients induce a static deflection and if this needs to be compensated, we need to apply a static control voltage and the magnitude of the static control voltage needed are quite high even for a smaller thermal gradient. The deflection induced due to thermal gradient, being a static load cannot be controlled by the negative velocity feedback control method, which is effective only for dynamic control.

Although the high-order displacement field is applicable to both thin and moderately thick beams, the interlaminar stresses are omitted which can cause premature structural failure. In order to avoid this failure, the layerwise displacement theory, which exploits the laminate architecture to separate the thickness variation from the surface variations, assuming a polynomial approximation for the distribution of the displacement field along the thickness within each ply, should be a good approach.

References

[1] E.F. Crawley, J. de Luis, Use of piezoelectric actuators as elements of intelligent structures, *AIAA Journal* 25 (1987) 1373–1385.

[2] H.S. Tzou, M. Gadre, Theoretical analysis of a multi-layered thin shell coupled with piezoelectric shell actuators for distributed vibration controls, *Journal of Sound and Vibration* 132 (1989) 433–450.

[3] B.T. Wang, C.A. Rogers, Laminate plate theory for spatially distributed induced strain actuators, *Journal of Composite Materials* 25 (1991) 433–452.
[4] C.K. Sung, T.F. Chen, S.G. Chen, Piezoelectric modal sensor/actuator design for monitoring /generating flexural and torsional vibrations of cylindrical shells, *Journal of Vibration and Acoustics* 118 (1996) 48–55.
[5] J.A. Mitchell, J.N. Reddy, A refined hybrid plate theory for composite laminates with piezoelectric laminae, *International Journal of Solids and Structures* 32 (1995) 2345–2367.
[6] H.S. Tzou, C.I. Tseng, Distributed piezoelectric sensor/actuator design for dynamic measurement/control of distributed parameter systems: a piezoelectric finite element approach, *Journal of Sound and Vibration* 138 (1990) 17–34.
[7] D.A. Saravanos, P.R. Heyliger, Coupled layerwise analysis of composite beams with embedded piezoelectric sensors and actuators, *Journal of Intelligent Material Systems and Structures* 6 (1995) 350–363.
[8] P.R. Heyliger, K.C. Pei, D.A. Saravanos, Layerwise mechanics and finite element model for laminated piezoelectric shells, *AIAA Journal* 34 (1996) 2353–2360.
[9] H.S. Tzou, Y. Bao, A theory on anisotropic piezothermoelastic shell laminates with sensors/actuator applications, *Journal of Sound and Vibration* 184 (1995) 453–473.
[10] K. Chandrashekhara, R. Tenneti, Thermally induced vibration suppression of laminated plates with piezoelectric sensors and actuators, *Smart Materials & Structures* 4 (1995) 281–290.
[11] M. Sunar, S.S. Rao, Piezothermoelastic control design and actuator placement, *AIAA Journal* 35 (1997) 534–539.
[12] T.R. Tauchert, F. Ashida, N. Noda, S. Adali, V. Verijenko, Developments in thermo-piezoelasticity with relevance to smart composite structures, *Composite Structures* 48 (2000) 31–38.
[13] A. Chattopadhyay, L. Jingmei, G. Haozhong, A coupled thermo-piezoelectric-mechanical model for smart composite laminates, AIAA-98-2044.
[14] L. Jingmei, Z. Xu, G. Haohong, A. Chattopadhyay, Dynamic responses of smart composites using a coupled thermo-piezoelectric-mechanical model, AIAA-99-1481.
[15] D. HaoJiang, G. FengLin, H. PengFei, A general solution for piezothermoelasticity of transversely isotropic piezoelectric materials and its applications, *International Journal of Engineering Science* 38 (2000) 1415–1440.
[16] G.A. Altay, M.C. Dökmeci, A non-linear rod theory for high-frequency vibrations of thermopiezoelectric materials, *International Journal of Non-linear Mechanics* 37 (2002) 225–243.
[17] G. Song, X. Zhou, W. Binienda, Thermal deformation compensation of a composite beam using piezoelectric actuators, *Smart Materials & Structures* 13 (2004) 30–37.
[18] G.A. Altay, M.C. Dökmeci, The consistent Mindlin's thermopiezoelectric equations and the principle of virtual work, *Mechanics Research Communications* 32 (2005) 115–119.
[19] G.A. Altay, M.C. Dökmeci, Fundamental variational equations of discontinuous piezothermoelastic fields, *International Journal of Engineering Science* 34 (7) (1996) 769–782.
[20] A. Benjeddou, O. Andrianarison, A piezothermoelastic mixed variational theorem for smart multilayered composites, *Computers & Structures* 83 (2005) 1266–1276.
[21] C.Y.K. Chee, L. Tong, P.G. Steven, A mixed model for composite beams with piezoelectric actuators, sensors, *Smart Materials & Structures* 8 (1999) 417–432.
[22] P. Bisegna, F. Maceri, An exact three-dimensional solution for simply supported rectangular piezoelectric plate, *Journal of Applied Mechanics* 63 (1996) 628–638.
[23] J.S. Yang, Equations for thick elastic plates with partially electroded piezoelectric actuators and higher order electric field, *Smart Materials & Structures* 8 (1999) 73–82.
[24] W.S. Hwang, H.C. Park, Finite element modeling of piezoelectric sensors and actuators, *AIAA Journal* 31 (1993) 930–937.
[25] H.S. Tzou, R. Ye, Analysis of piezoelastic structures with laminated piezoelectric triangle shell elements, *AIAA Journal* 34 (1996) 110–115.
[26] J.G. Smits, S.I. Dalke, T.K. Cooney, The constituent equations of piezoelectric bimorphs, *Sensors and Actuators A* 28 (1991) 41–61.
[27] G.E. Blandford, T.R. Tauchert, Y. Du, Self-strained piezothermoelastic composite beam analysis using first-order shear deformation theory, *Composites: Part B* 30 (1999) 51–63.